

Depolarization-Field-Induced Retention Loss in Ferroelectric Diodes


Junjiang Tian,^{1,2} Zhengwei Tan,^{1,3} Zhen Fan,^{1,2,*} Dongfeng Zheng,¹ Yadong Wang,¹ Zoufei Chen,¹ Fei Sun,¹ Deyang Chen,^{1,2} Minghui Qin,^{1,3} Min Zeng,^{1,3} Xubing Lu,^{1,3} Xingsen Gao,^{1,3} and Jun-Ming Liu^{1,3,4}

¹*Institute for Advanced Materials, South China Academy of Advanced Optoelectronics, South China Normal University, Guangzhou 510006, China*

²*Guangdong Provincial Key Laboratory of Optical Information Materials and Technology, South China Academy of Advanced Optoelectronics, South China Normal University, Guangzhou 510006, China*

³*Guangdong Provincial Key Laboratory of Quantum Engineering and Quantum Materials, South China Academy of Advanced Optoelectronics, South China Normal University, Guangzhou 510006, China*

⁴*Laboratory of Solid State Microstructures and Innovation Center of Advanced Microstructures, Nanjing University, Nanjing 210093, China*

 (Received 2 April 2018; revised manuscript received 30 January 2019; published 22 February 2019)

For recently emerging ferroelectric resistive memories, for example, ferroelectric diodes, retention is one of the most critical concerns and understanding its underlying physics is of importance. It is proposed that in a ferroelectric diode, the depolarization field (E_{dp})-driven polarization relaxation can modify the conduction against time, because the metal/ferroelectric Schottky barrier is greatly influenced by the polarization. Based on this effect, a theoretical model combining both the E_{dp} -driven polarization relaxation kinetics and polarization-controlled Schottky emission is established. Simultaneously, we experimentally investigate the retention characteristics of the metal/BiFeO₃ (BFO)/La_{0.7}Sr_{0.3}MnO₃ (LSMO) ferroelectric diodes with various BFO thicknesses and top electrodes in order to verify this model. It is revealed that all the samples exhibit switchable diodelike resistive switching behaviors. The measured current-time [$I(t)$ - t] characteristics show that the current in the low-resistance state decreases with time, indicating resistance relaxation. Moreover, the resistance relaxation becomes faster as the BFO thickness decreases from 40 to 10 nm and as the top electrode changes from Ag to Au and to Co. Using appropriate parameters, all the $I(t)$ - t characteristics and their dependences on the BFO thickness and the top electrode's screening ability can be well described by the proposed retention model, in which the key role of the E_{dp} is demonstrated. It is, therefore, deduced that the retention loss in a ferroelectric diode is mainly caused by the E_{dp} -driven polarization relaxation and its effects on the Schottky emission. In addition to these fundamental insights, our study also provides suggestions for the technical aspects, such as improving the retention properties and nondestructively monitoring the polarization over time.

DOI: [10.1103/PhysRevApplied.11.024058](https://doi.org/10.1103/PhysRevApplied.11.024058)

I. INTRODUCTION

Ferroelectric random-access memory (FERAM) has been considered as a competitive candidate for next-generation nonvolatile memories owing to its fast writing speed, high cycling endurance, and low power consumption [1], but its commercial applications are limited by the destructive readout scheme. Recent discoveries of ferroelectric resistive switching (FERS) phenomena, such as those observed in ferroelectric diodes [2–4], ferroelectric tunnel junctions [5–8], and domain walls [9–13], may offer a unique nondestructive resistive readout scheme. Unlike conventional resistive switching (RS) memories making use of defects-mediated processes

[14–17], the FERS is, in principle, a pure electronic process and may possess a fundamental merit in terms of reliability and write-read speed. For example, in ferroelectric diodes, the polarization can modulate the height and width of a ferroelectric/electrode interfacial Schottky barrier [4,18,19], giving rise to polarization-dependent high- and low-resistance states. However, the polarization relaxation remains a crucial issue and becomes increasingly important when thinning the ferroelectric films [20,21]. This, in turn, leads to the retention loss of resistance states in the FERS memories. Despite being a key performance indicator, the retention of FERS, in particular its underlying physics, is not well understood.

Generally, researchers have characterized the retention properties of their FERS devices by measuring the resistances in *on* and *off* states as a function of time

*fanzhen@m.scnu.edu.cn

(typically up to 10^2 – 10^6 s) [3,22–24]. If there was no significant reduction of the *on:off* resistance ratio in that time range, the retention was claimed to be “good”. Some researchers further predicted the resistances retained after 10 years (approximately 3×10^8 s; the required shelf life of a memory cell) by linearly extrapolating the resistance-time $[R(t)-t]$ curves in the log-log plots [25,26]. In fact, those claims and predictions were empirical and lacked physical justifications, because no quantitative models describing the $R(t)-t$ relationships have been available so far. Only with such models in hand can one reasonably fit the retention data and give a prediction. Moreover, these models may shed light on how to improve the retention properties, which is essential for developing highly stable FERS devices.

Up until now, a consensus has been reached that the depolarization field (E_{dp}), which is formed by the incomplete screening at the ferroelectric/electrode interface, is the main cause of polarization relaxation in epitaxial ferroelectric films [20,21]. It is noted that some defects-related factors can also cause polarization relaxation, such as non-switchable interfacial layers [27], grain boundaries [28], and defects dipoles [29,30]. However, their roles become insignificant in high-quality epitaxial films. In addition, the built-in field near the ferroelectric/electrode interface may also lead to polarization relaxation [31], but it is unidirectional and can be distinguished from the issue under study in this paper. Therefore, we focus mainly on the polarization relaxation induced by the E_{dp} . The E_{dp} can further cause retention loss in the FERS devices due to the aforementioned polarization-controlled conduction, which has been qualitatively proved by several experimental observations. For example, Pantel *et al.* [22] observed that in the $\text{Cu/Pb}(\text{Zr}_{0.2}\text{Ti}_{0.8})\text{O}_3/\text{La}_{0.7}\text{Sr}_{0.3}\text{MnO}_3$ ferroelectric diodes, the polarization underwent a back switching driven by the E_{dp} within several tens of seconds, accompanied by a concurrent reduction of *on*-state current. Kim *et al.* [32] reported a faster relaxation of the *on:off* resistance ratio in the $\text{Co/BaTiO}_3/\text{La}_{2/3}\text{Sr}_{1/3}\text{MnO}_3$ ferroelectric tunnel junctions with thinner BaTiO_3 films where a larger E_{dp} exists. However, the quantitative correlations between E_{dp} , polarization, and resistance have not been investigated either theoretically or experimentally. These correlations in combination with the polarization relaxation kinetics are of importance for establishing the retention model for the FERS devices.

Likewise, by correlating the polarization and resistance, one may be able to use the $R(t)-t$ measurements as a viable approach to nondestructively monitor the polarization over time. Note that the conventional polarization retention tests rely on the pulse methods [20,21,33], which are destructive. Additionally, compared to the pulse methods, the $R(t)-t$ measurements have less stringent requirements for the insulativity of a material, which may be extremely useful for leaky ferroelectrics and ultrathin films.

In this paper, we first develop a retention model for ferroelectric diodes on the basis of the E_{dp} -driven polarization relaxation kinetics and the conduction mechanism of Schottky emission, which is polarization controlled. We then prepare a series of metal/ BiFeO_3 (BFO)/ $\text{La}_{0.7}\text{Sr}_{0.3}\text{MnO}_3$ (LSMO) ferroelectric diodes with various BFO thicknesses and top electrodes, which all show switchable diodelike RS behaviors. The experimentally observed retention characteristics can be well described by our model, demonstrating the validity of this model. In addition, our model can explain the dependences of the resistance-relaxation rate on the BFO thickness and the top electrode’s screening ability by taking into account the role of E_{dp} .

II. THEORETICAL FORMALISM

The proposed retention model combines the E_{dp} -driven polarization relaxation kinetics and the polarization-controlled Schottky emission, which will be described in detail below.

A. Depolarization field

A ferroelectric capacitor consists of a metal/ferroelectric/metal (MFM) structure, as shown in Fig. 1(a). For an electrically poled ferroelectric film having macroscopic polarization P , two sheets of polarization charges ($\pm P$) appear on the M/F interfaces. To compensate for the polarization charges, the screening charges ($\pm\sigma_s$) are built up in the metals near the M/F interfaces. In realistic metals, however, the screening charges are displaced for finite distances from the interfaces, leading to the incomplete screening of polarization charges [34]. Consequently, the E_{dp} arises, which is given by

$$E_{dp} = \frac{-(P - \sigma_s)}{\epsilon_0 \epsilon_{st}}. \quad (1)$$

Here, ϵ_0 is the vacuum permittivity and ϵ_{st} is the static dielectric constant of the ferroelectric layer. In Eq. (1), the negative sign in front of $(P - \sigma_s)$ indicates that the direction of E_{dp} is opposite to that of the polarization. Unless otherwise specified, we will neglect the negative sign and consider only the magnitude of E_{dp} . Note that Eq. (1) applies to the case where the interfacial trapped charges are minor factors, which may be neglected. [See Appendix A for more details.]

The remaining task is to figure out the σ_s . Assuming that the screening is of the Thomas-Fermi type, we obtain [35]

$$\sigma_s = \frac{Pd}{\epsilon_{st}[(l_1/\epsilon_{M,1}) + (l_2/\epsilon_{M,2})] + d}, \quad (2)$$

where d is the thickness of the ferroelectric film, $l_{1(2)}$ is the screening length of electrode $M_{1(2)}$, and $\epsilon_{M,1(2)}$ is the

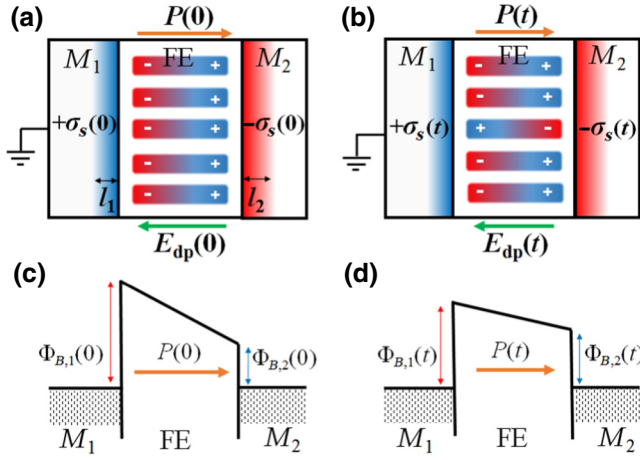


FIG. 1. Schematics of MFM structures showing (a) the alignment of all the domains along one direction right after applying the external field (i.e., initial state) and (b) the back switching of certain domains after a certain time (i.e., polarization-relaxed state). The schematic energy-band diagrams corresponding to (c) the initial state and (d) the polarization-relaxed state. Here, the potential distributions within the metals are not drawn.

permittivity of electrode $M_{1(2)}$. The electrodes M_1 and M_2 correspond to the bottom and top electrodes, respectively. For an ideal conductor, the screening length is zero while the dielectric constant is infinity. In this case, the σ_s equals the P [see Eq. (2)], and therefore, the E_{dp} is zero [see Eq. (1)]. For a realistic metal, however, its screening length and dielectric constant have finite values. This causes the σ_s to be smaller than the P [see Eq. (2)], that is, incomplete screening, and, in turn, leads to the presence of E_{dp} [see Eq. (1)].

B. Polarization relaxation

As seen above, for realistic MFM structures, the E_{dp} unavoidably exists, which can drive the back switching of certain polarizations, giving rise to the polarization relaxation [Fig. 1(b)]. To describe such E_{dp} -driven polarization relaxation, we apply a model proposed by Lou [36]. This model assumes that the back switching occurs in a region-by-region manner, as observed in both polycrystalline and epitaxial ferroelectric films [37–40]. More specifically, a ferroelectric film can be divided into N_0 ($N_0 \gg 1$) elementary regions. The back switching of a region is realized by the nucleation and growth of the reversed domain until it fills up the whole region. The events of back switching in different regions are independent. As time goes by, the number of back-switched regions increases, and therefore, the retained polarization decreases. This, in turn, leads to the change of E_{dp} (i.e., the driving force for back switching) with time [see Eq. (1)]. In other words, both $P(t)$ and $E_{dp}(t)$ are functions of time. The key idea of Lou's model is to use a feedback loop of the E_{dp} corrected by the updated

retained polarization at each time point to derive $P(t)$ and $E_{dp}(t)$ [36].

While the detailed derivation can be found in Ref. [36], we present here only the resultant feedback equations:

$$\frac{N_0 - 1}{N_0} = \exp \left\{ -\frac{\Delta t_1}{t_\infty} \times \exp \left[-\frac{\alpha}{E_{dp}(t_0)} \right] \right\}, \quad (3)$$

$$\frac{N_0 - 2}{N_0 - 1} = \exp \left\{ -\frac{\Delta t_2}{t_\infty} \times \exp \left[-\frac{\alpha}{E_{dp}(t_1)} \right] \right\}, \quad (4)$$

...

$$\frac{N_0 - n}{N_0 - n + 1} = \exp \left\{ -\frac{\Delta t_n}{t_\infty} \times \exp \left[-\frac{\alpha}{E_{dp}(t_{n-1})} \right] \right\}. \quad (5)$$

...

Equations (3) and (4) describe the back switching of the first and second regions, respectively. By analogy, Eq. (5) describes the back switching of the n th region with $n = [1, 2, \dots, (N_0/2) - 1]$. Δt_n is the time interval that the n th region takes to back switch, while t_n is the total time required for the back switching of all n regions, which can be written as

$$t_n = t_0 + \sum_{i=1}^n \Delta t_i. \quad (6)$$

Additionally, in Eqs. (3)–(5), t_∞ is the switching time under an infinite field and α is the activation field for switching. Both t_∞ and α are the parameters of the Merz equation

$$\frac{1}{t_{sw}} = \frac{1}{t_\infty} \times \exp \left(-\frac{\alpha}{E} \right), \quad (7)$$

where t_{sw} is the switching time under the field E . In Eq. (7), $1/t_{sw}$ can be interpreted as the probability per unit time of the polarization switching under the field E . Therefore, by comparing Eq. (7) and Eqs. (3)–(5), one can find that the back switching is nothing more than the polarization switching driven by a time-dependent depolarization field $E_{dp}(t)$.

If the initial polarization at t_0 (the moment when the external field is just removed) is P_0 , the retained polarization $P(t_n)$ after the back switching of n regions can be expressed as

$$P(t_n) = \frac{N_0 - 2n}{N_0} P_0. \quad (8)$$

Now the polarization relaxation kinetics can be quantitatively determined by solving Eqs. (1)–(8) iteratively. For example, once $P(t_{n-1})$ is known, then $E(t_{n-1})$ can be calculated using Eqs. (1) and (2). Substituting $E(t_{n-1})$ into Eq. (5), one can calculate Δt_n and further obtain t_n using Eq. (6). Since $P(t_n)$ can be straightforwardly known from Eq. (8), the $P(t_n)$ - t_n relationship is thus established.

C. Conduction mechanism

The remaining task is to establish the relationship between polarization and resistance by analyzing the conduction mechanisms. In the concerned ferroelectric diodes, the ferroelectric layers are intermediately thick (typically several tens of nanometers) and semiconducting (assuming n type hereafter), which can form two Schottky barriers ($\Phi_{B,1}$ and $\Phi_{B,2}$) with the bottom (M_1) and top (M_2) electrodes, respectively [Fig. 1(c)]. In these structures, the Schottky emission, manifested as the injection of thermally activated electrons across the Schottky barrier into the conduction band of the ferroelectric film, may be the major conduction mechanism, noting that other conduction mechanisms may also be involved (to be discussed later). The current flow is mainly controlled by the barrier that is reverse biased, which depends on the polarity of the applied voltage V . For example, if V applied on the top electrode is negative, the top barrier $\Phi_{B,2}$ is reverse biased and thus limits the overall current. The current due to Schottky emission at the reverse-biased barrier is given by [18,19]

$$I = SA^*T^2 \exp \left[-\frac{q}{k_B T} \left(\Phi'_B - \sqrt{\frac{qE}{4\pi\epsilon_0 K}} \right) \right], \quad (9)$$

where S is the electrode area, A^* is the Richardson constant, q is the electron charge, T is the absolute temperature, k_B is the Boltzmann constant, K is the optical dielectric constant of the ferroelectric, and E is the electric field ($E = V/d$, assuming that the film is fully depleted). Φ'_B is the apparent Schottky barrier height, which may be expressed as [18,41]

$$\Phi'_B = \Phi_B^0 - \left(\frac{q^3 N_{\text{eff}} V_{\text{bi}}}{8\pi^2 \epsilon_0^3 K^2 \epsilon_{\text{st}}} \right)^{1/4} \pm \sqrt{\frac{qP}{4\pi \epsilon_0^2 K \epsilon_{\text{st}}}}, \quad (10)$$

where Φ_B^0 is the Schottky barrier height determined purely by the difference of the electrode's work function and the ferroelectric's electron affinity, N_{eff} is the space charge density, and V_{bi} is the built-in voltage. The second and third terms on the right-hand side of Eq. (10) represent the barrier height modulations by the space charges and polarization charges, respectively. The positive (negative) sign in front of the third term is adopted when the negative (positive) polarization charge is located at this barrier. In other words, the negative (positive) polarization charge increases (decreases) the apparent Schottky barrier height, giving rise to the polarization-controlled Schottky emission.

As seen from Eqs. (9) and (10), the polarization relaxation can cause the barrier height variation [Figs. 1(c) and 1(d)], and, in turn, leads to the current relaxation. Since the $P(t)$ - t relationship has been already established

(see the previous section), the $I(t)$ - t [or $R(t)$ - t , equivalently] relationship can also be obtained via Eqs. (9) and (10).

Note that when the mean free path of the ferroelectric film is small, the charge transport may become bulk limited, and therefore, the conduction mechanisms may be changed. In such a case, Eq. (9) may be modified into the Simmons equation [41] to more appropriately describe the current. However, we still use Eq. (9) in this work because of the following two reasons. First, the reported mean free paths in epitaxial ferroelectric films (approximately 20 nm) [41] are comparable to the thicknesses of the films being investigated in this work, suggesting that Eq. (9) may still be applicable. Second, Eq. (9) and the Simmons equation are similar in form, and the only difference is that the pre-exponential term in the Simmons equation is weakly field dependent [41]. For the problem of interest in this work, a small and constant read voltage is applied during the retention test. Therefore, for modeling the $I(t)$ - t relationships, using Eq. (9) or the Simmons equation would make little difference.

III. EXPERIMENTAL METHOD

The BFO/LSMO bilayers are grown on the (001) SrTiO₃ (STO) single-crystal substrates by pulsed laser deposition (PLD) using a KrF excimer laser ($\lambda = 248$ nm). The 40-nm-LSMO films are grown at 650 °C under an oxygen pressure of 15 Pa. Subsequently, the BFO films with thicknesses of 10, 20, 30, and 40 nm are grown at 690 °C under an oxygen pressure of 13 Pa. After deposition, the samples are cooled down to room temperature at 10 °C/min in an oxygen ambient atmosphere of 1 atm.

The crystal structures of the samples are characterized by XRD and further checked by TEM. The topography, ferroelectricity, conduction, and surface potential are studied by AFM, piezoresponse force microscopy (PFM), conductive AFM (CDAFM), and scanning Kelvin probe microscopy (SKPM), respectively, all of which are based on a commercial AFM (Cypher, Asylum Research). In the CDAFM measurements, the nanosized Au, Ag, and Co top electrodes (approximately 0.15 μm^2 in area) are deposited by a thermal evaporation method using the polystyrene spheres as templates.

A representative 30-nm-BFO film is used to demonstrate the good quality of our samples. Figure 2(a) reveals that the BFO film is atomically flat, with a roughness of approximately 200 pm. The XRD θ - 2θ scan in Fig. 2(b) shows the distinct (00 l) diffraction peaks from only BFO, LSMO, and STO, indicating the phase purity. Figure 2(c) presents the reciprocal space mapping (RSM) around the (113) reflection, in which H , K , and L are the reciprocal space coordinates. As clearly seen, the (113) diffraction spot of BFO does not split and it almost has the same H coordinate as those of LSMO and STO. These observations suggest that the 30-nm-BFO film is almost fully

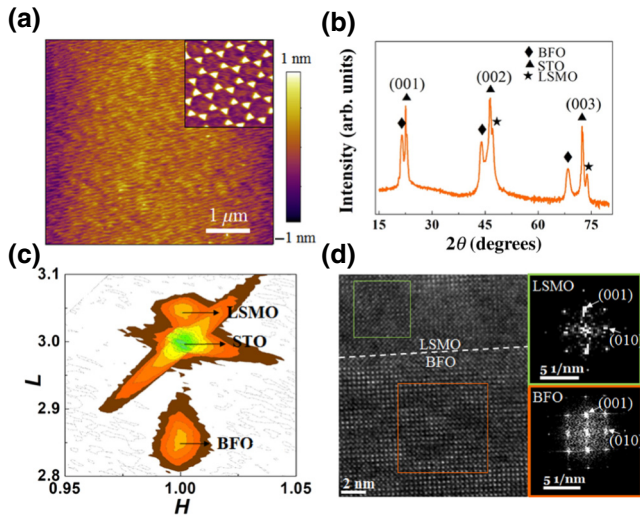


FIG. 2. (a) AFM topography image of the 30-nm-BFO film. Inset shows the topography image taken after growing Au nanodots as top electrodes. (b) XRD θ - 2θ scan and (c) RSM around the (113) reflection of the BFO(30 nm)/LSMO/STO heterostructure. (d) High-resolution TEM image taken at the BFO/LSMO interface and FFT patterns of BFO and LSMO.

strained and exhibits a tetragonal-like structure without monoclinic tilting [42]. The high-resolution TEM image [Fig. 2(d)] further demonstrates the high-quality BFO and LSMO epitaxial layers with a flat interface. Combining the FFT pattern [inset in Fig. 2(d)] and the above XRD and RSM results, the lattice parameters of BFO are calculated as: $c \sim 4.10$ Å and $a \sim 3.91$ Å.

IV. RESULTS AND DISCUSSION

A. Ferroelectric properties

Figure 3(a) displays the PFM phase and amplitude hysteresis loops of the 30-nm-BFO film. The phase is switched by approximately 180° and the amplitude loop exhibits a butterflylike shape, demonstrating the ferroelectric nature. In addition, the PFM out-of-plane phase image [Fig. 3(b)], which was taken immediately after electrically writing two adjacent areas with tip biases of +9 and -9 V, shows a clear phase contrast of approximately 180° . This signifies the formation of antiparallel domains in the two areas, providing evidence for the ferroelectric switching. However, the phase image [Fig. 3(c)] taken 10 min after the electrical writing shows a decay in the phase contrast, suggesting that polarization relaxation exists in the BFO film. Figure 3(d) further shows the time-dependent amplitudes measured in the +9 and -9 V written areas. As can be seen, both upward and downward polarizations (i.e., P_{up} and P_{down}) do relax. From this observation, and also considering the high quality of the epitaxial BFO films, one may infer that the polarization relaxation is mainly caused by the E_{dp} rather than the unidirectional built-in field or the defects-related factors.

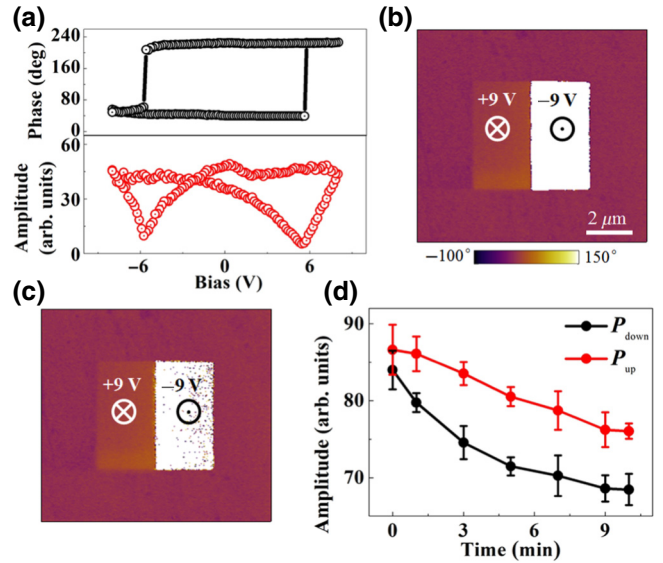


FIG. 3. (a) PFM phase (upper panel) and amplitude (lower panel) hysteresis loops of the 30-nm-BFO film. PFM phase images taken (b) right after the electrical writing and (c) after waiting for 10 min. (d) Time-dependent amplitudes measured in the +9 and -9 V written areas (corresponding to P_{down} and P_{up} , respectively).

B. I - V and $I(t)$ - t characteristics of the Au/BFO(30 nm)/LSMO structure

The Au nanodots (approximately $0.15 \mu\text{m}^2$ in area) are used as the top electrodes for the CDAFM measurements. The bottom electrodes are the LSMO films, which exhibit metallic-conduction behaviors (see results in Appendix B). Figure 4(a) shows the typical current-voltage (I - V) characteristics of the Au/BFO(30 nm)/LSMO structure. The sequence of voltage sweep is $-8 \text{ V} \rightarrow 0 \rightarrow +8 \text{ V} \rightarrow 0 \rightarrow -8 \text{ V}$ (sweep rate: 0.1 Hz), and the voltage is termed as positive when the top electrode is positively biased. In Fig. 4(a), a clear switchable diodelike RS behavior is observed, and the voltages where the high-resistance state (HRS) changes to the low-resistance state (LRS) coincide with the coercive voltages (approximately -5.7 and $+5.8$ V) [see comparison between the upper and lower panels in Fig. 4(a)]. Such RS behavior is, however, not observed in the STO films, which are nonferroelectric (see results in Appendix C). Therefore, the RS is most likely to be caused by the polarization reversal in the BFO films.

More specifically, as the voltage sweeps from -8 to $+5.8$ V, the polarization is oriented upward, increasing the barrier height at the BFO/LSMO interface while reducing that at the Au/BFO interface [assuming that BFO is an n type semiconductor; see Eq. (10)]. Due to the asymmetric barrier heights, the electron emission across the top (bottom) barrier is facilitated (suppressed), resulting in larger currents at negative voltages than at positive voltages (i.e., diodelike current rectification), as shown by the red curve

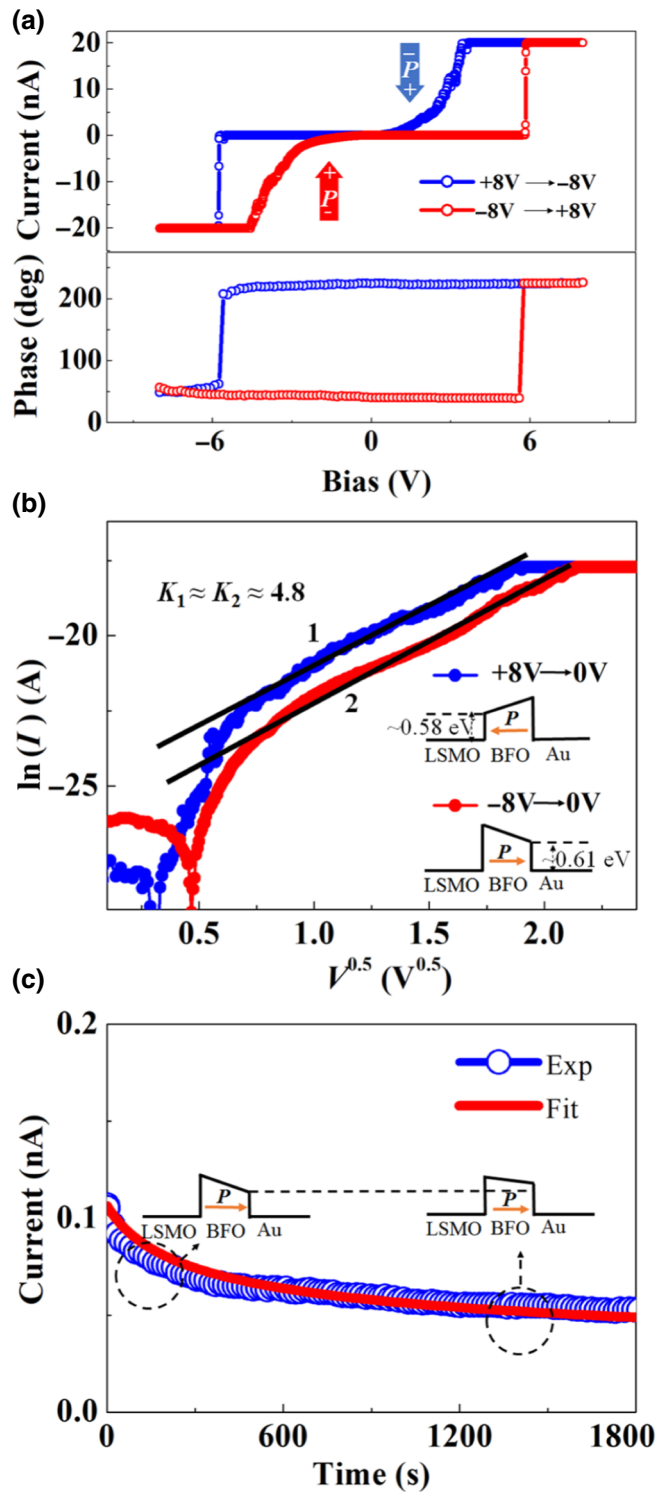


FIG. 4. Conduction measurements on the Au/BFO(30 nm)/LSMO structure. (a) Typical I - V characteristics (upper panel) and PFM phase loop (lower panel). (b) Plots of $\ln(I)$ vs $V^{0.5}$ in the voltage ranges of $-8\text{ V} \rightarrow 0$ and $+8\text{ V} \rightarrow 0$. Insets show the schematics of Schottky barriers in the P_{up} and P_{down} states. (c) Experimental data of the $I(t)$ - t characteristics and the fitting curve calculated from our retention model. Insets schematically show the variation of barrier heights over time.

in Fig. 4(a). When the voltage exceeds $+5.8\text{ V}$, the polarization is switched downward and thus the asymmetry of the top and bottom barrier heights is reversed. This leads to the reversal of the diode's forward direction, which is maintained during the voltage sweep from $+8\text{ V}$ back to -5.7 V [see blue curve in Fig. 4(a)].

One prerequisite for the above scenario (i.e., RS induced by the polarization-controlled Schottky emission) is that the Schottky emission is truly the major conduction mechanism. To verify it, the I - V curves in the LRS are replotted in the form of $\ln(I)$ vs $V^{0.5}$ [see Eq. (9)], as shown in Fig. 4(b). The $\ln(I)$ - $V^{0.5}$ curves under both $-8\text{ V} \rightarrow 0$ and $+8\text{ V} \rightarrow 0$ exhibit certain linearity, implying that the conduction is governed by the Schottky emission. Moreover, the optical dielectric constants calculated from the slopes of the fitting lines are approximately 4.8, which agree with the experimental value of BFO (approximately 6.25) [43]. This indicates the validity of the Schottky emission model. The barrier heights can also be estimated using the intercepts of fitting lines on the $\ln(I)$ axis. In the voltage range of $-8\text{ V} \rightarrow 0$, the Au/BFO barrier limits the current and its height is approximately 0.61 eV ; however, as the voltage sweeps from $+8\text{ V}$ to 0 , the BFO/LSMO barrier is current limiting and its height is approximately 0.58 eV [see insets in Fig. 4(b)]. Note that the I - V characteristics in the HRS are not used for fitting, because the measured currents are very low and contain significant contributions from capacitive currents and background noises. Therefore, the heights of current-limiting barriers in the HRS (i.e., Au/BFO and BFO/LSMO barriers in the voltage ranges of $0 \rightarrow -5.7\text{ V}$ and $0 \rightarrow +5.8\text{ V}$, respectively) are unavailable. More detailed results and analyses, which confirm the Schottky emission mechanism and verify the Schottky barrier heights, are provided in Appendix D.

The retention behavior of the Au/BFO(30 nm)/LSMO structure is investigated by measuring the current at a small read voltage of -1 V after applying a -8 V write pulse to set the P_{up} state (i.e., the LRS is achieved and the Au/BFO barrier is current limiting). Note that the retention test is not applicable for the HRS because of the issues associated with the low currents, as mentioned above. In addition, only the magnitude of the current will be used while its sign will be neglected hereafter. As shown in Fig. 4(c), the current decays relatively quickly (from approximately 0.1 nA to approximately 0.07 nA) within the first 300 s , and then slowly decreases to approximately 0.05 nA at 1800 s . Such current decay behavior is reproducible, as demonstrated in the cyclic retention tests (see results in Appendix E).

The current decay is not caused by the capacitive current resulting from the polarization relaxation, because the capacitive current is several orders of magnitude lower than the current shown in Fig. 4(c) (see Appendix E for comparison). Hence, the current measured at -1 V in the retention test is mainly the conductive current, which is

time dependent, and the current decay indicates that the resistance increases over time. It is also demonstrated that such resistance relaxation is not caused by the defect-mediated charge-trapping processes (see Appendix F for more details). In addition, the resistance relaxation is not observed in the nonferroelectric STO films (see results in Appendix C). Therefore, the resistance relaxation observed in the Au/BFO/LSMO structure is most probably due to the relaxation of the BFO's polarization, which induces the Schottky barrier variation during the conduction. Moreover, the resistance relaxation is also observed in the LRS in the P_{down} state (see results in Appendix G), suggesting that its main driving force is the E_{dp} rather than the built-in field.

To further understand the mechanism of resistance relaxation, we use the model proposed in Sec. II [Eqs. (1)–(10)] to fit the observed $I(t)$ - t characteristics. In the fitting procedures, some parameters that were taken from the literature are fixed: for BFO, $\varepsilon_{\text{st}} = 60$ [19], $K = 6.25$ [43], $t_{\infty} = 1$ ns [36], and $P(t=0) = 60 \mu\text{C}/\text{cm}^2$ [44]; for LSMO, $l_1 = 0.8 \text{ \AA}$ and $\varepsilon_{M,1} = 8$ [19]. Additionally, some parameters determined from the experiment data are also fixed [e.g., $\Phi'_{B,2}(t=0) = 0.61 \text{ eV}$ for the Au/BTO barrier, which is current limiting]. Other parameters, which depend on the film thickness (activation field α) and the top electrode (l_2 and $\varepsilon_{M,2}$), are varied to obtain good fits. All parameters used for the fittings are summarized in Table I in Appendix H. As clearly seen from Fig. 4(c), the experimental $I(t)$ - t curve can be well fitted and the fitting parameters are obtained as: $\alpha = 2.19 \times 10^9 \text{ V/m}$, $l_2 = 0.5 \text{ \AA}$, and $\varepsilon_{M,2} = 2$. It is typical that the α value is one order of magnitude higher than the coercive field (E_c) [45], that is, approximately $2 \times 10^8 \text{ V/m}$ in our 30-nm-BFO film as indicated by the PFM results [Fig. 3(a)]. (Note that this large E_c is reasonable for the BFO at such a small thickness because the reported E_c values of the > 100 -nm-BFO films are 0.1 to $0.5 \times 10^8 \text{ V/m}$ [44,46], while they became as large as 2 to $7 \times 10^8 \text{ V/m}$ in the < 10 -nm-BFO films [26,47].) In addition, the l_2 and $\varepsilon_{M,2}$ values are consistent with those reported for Au [19]. All the results demonstrate the validity of our model. As our model suggests, the E_{dp} -driven polarization relaxation [Eqs. (3)–(8)] can increase the height of the Au/BFO barrier over time [Eqs. (9) and (10)]. This appears to be the origin for the resistance relaxation [see insets in Fig. 4(c)].

C. $I(t)$ - t characteristics of metal/BFO/LSMO structures with different BFO thicknesses and top electrodes

To further verify this origin, the retention properties of metal/BFO/LSMO ferroelectric diodes with different BFO thicknesses and top electrodes are studied. In the retention tests, the write and read operations are the

same for all the structures, as described for the above Au/BFO(30 nm)/LSMO structure.

The I - V characteristics in the insets of Figs. 5(a)–5(d) illustrate that the BFO films with thicknesses of 10, 20, 30, and 40 nm all exhibit switchable diodelike RS behaviors. Figures 5(a)–5(d) also show the normalized $I(t)$ - t characteristics, from which one can see that the current decays more rapidly in thinner BFO films. Furthermore, all the normalized $I(t)$ - t characteristics are well fitted to the proposed retention model by varying only the thickness-dependent parameter (activation field α) while keeping the other parameters unchanged. As shown in Fig. 5(e), the calculated E_{dp} increases as the BFO film becomes thinner, consistent with the known facts. The E_{dp} values appear to be quite large (0.6 to $1.9 \times 10^8 \text{ V/m}$), but they are still smaller than the E_c values. Although no measured E_{dp} values of BFO films are available, the work by Kim et al. [20] on BaTiO₃ (BTO) films, using the pulse methods, showed that the E_{dp} values of the 5 to 30-nm-BTO films are 0.3 to $0.8 \times 10^8 \text{ V/m}$, which are even comparable to the E_c values of those BTO films. Considering that our BFO films have similar thicknesses but larger polarizations compared to the BTO films, it is, therefore, plausible that the E_{dp} values of our BFO films are on the order of 10^8 V/m . As the BFO thickness decreases, the E_{dp} becomes larger

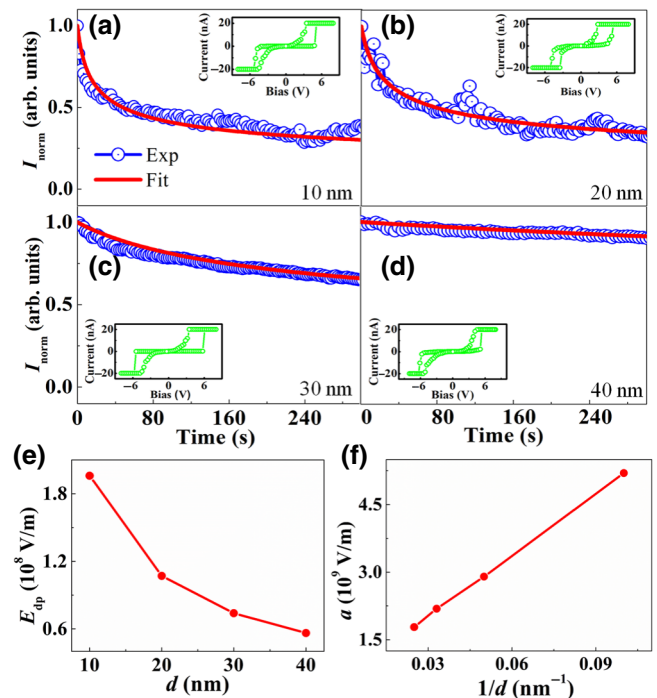


FIG. 5. Experimental and fitted normalized $I(t)$ - t characteristics of the (a) 10-nm-, (b) 20-nm-, (c) 30-nm-, and (d) 40-nm-BFO films. Insets show the corresponding I - V curves. (e) Depolarization field (E_{dp}) at $t=0$ as a function of BFO thickness (d). (f) Relationship between the activation field (α) and the reciprocal of BFO thickness ($1/d$).

and causes a faster polarization relaxation [Eqs. (3)–(8)], which is naturally correlated with the observed faster resistance relaxation in thinner BFO films. In addition, Fig. 5(f) reveals that the α is roughly proportional to the reciprocal of film thickness, agreeing well with the empirical relationship [48]. This confirms that the E_{dp} -driven polarization relaxation can be appropriately described by the Merz equation [Eq. (7)].

Figure 6(a) displays the normalized $I(t)$ - t characteristics of the 30-nm-BFO films with the Au, Co, and Ag top electrodes. As the top electrode changes from Ag to Au and to Co, the current decay becomes more significant. To understand this observation, the normalized $I(t)$ - t characteristics are fitted by using the retention model, in which only the top electrode-dependent parameters (l_2 and $\varepsilon_{M,2}$) are varied while the other parameters are fixed. As can be seen from Fig. 6(b), the fitted values of the screening length over permittivity ratios (i.e., $l_2/\varepsilon_{M,2}$) of Ag, Au, and Co are 2.4, 2.5, and 2.81 ($\times 10^{-11}$ m), respectively. Although the experimental values of l_2 and $\varepsilon_{M,2}$ are hardly known, one may qualitatively evaluate the screening ability of a metal

(which is inversely related to the $l_2/\varepsilon_{M,2}$ value) according to its conductivity. It is known that among the three metals of Ag, Au, and Co, the conductivity of Ag is the highest whereas that of Co is the lowest. Therefore, the $l_2/\varepsilon_{M,2}$ value may increase as the top electrode changes as Ag \rightarrow Au \rightarrow Co, which is consistent with the results shown in Fig. 6(b). According to Eqs. (1) and (2), a larger $l_2/\varepsilon_{M,2}$ gives rise to a larger E_{dp} , which is confirmed by the calculated E_{dp} values shown in Fig. 6(b). This can, therefore, explain the observed top-electrode dependence of resistance relaxation behavior. Note that such a dependence cannot be explained by the different work functions of top electrodes and associated built-in fields, because (i) the work functions of Ag, Au, and Co are approximately 4.6, 5.3, and 5.0 eV [49], respectively, which shows a trend different from that of the resistance relaxation rate; and (ii) the built-in field near the top interface is pointing upward, which is opposite to the direction of polarization relaxation.

D. Remarks about the retention model

As seen above, the magnitude of E_{dp} , which depends on the BFO thickness and the top electrode's screening ability, determines the rate of resistance relaxation. Because the E_{dp} plays an essential role and it has been fully expressed by our model (including its formation and its effects on the polarization relaxation and further on the conduction), our model can, therefore, successfully reproduce the experimental $I(t)$ - t characteristics. Note that our model is not limited to the ferroelectric diodes in the LRS, but can also be readily applied to the case of HRS if the Schottky barrier height is known. Therefore, one can predict the retention properties of the ferroelectric diodes over a long time period, for example, the *on:off* resistance ratios retained after 10 years.

In addition, our model suggests that in order to improve the retention properties, one needs to increase the film thickness and use the metals with short screening lengths and high permittivities as the top electrodes. However, those approaches may deteriorate the initial-state RS properties or even change the conduction mechanism away from Schottky emission. It is, therefore, necessary to make a trade-off between the retention and other RS properties. In addition, our model can be modified to suit other types of FERS. For example, the retention of ferroelectric tunnel junctions can also be modeled if the conduction mechanism of Schottky emission is replaced with quantum mechanical tunneling. Last but not the least, as the correlation between resistance and polarization is established in our model, the time-dependent resistance measurements may be used as a viable approach to nondestructively monitor the polarization over time. This may be particularly useful for leaky ferroelectrics and ultrathin films, as mentioned in the Introduction section.

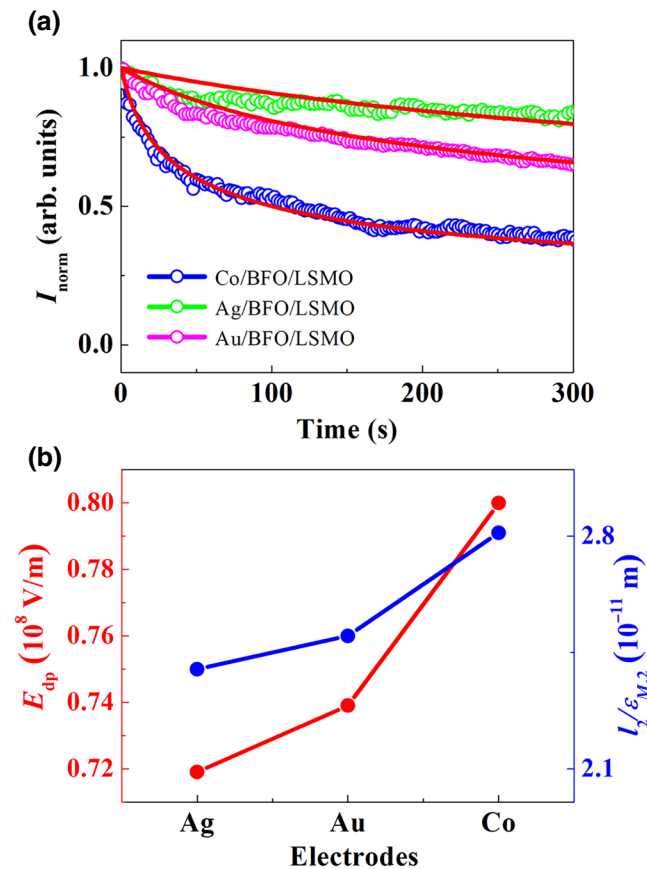


FIG. 6. (a) Experimental and fitted normalized $I(t)$ - t characteristics of the 30-nm-BFO film capped with the Ag, Au, and Co top electrodes. (b) Top-electrode dependences of the depolarization field (E_{dp}) at $t = 0$ and the screening length over permittivity ratio ($l_2/\varepsilon_{M,2}$).

V. CONCLUSION

In summary, by combining the theories of E_{dp} -driven polarization relaxation kinetics and polarization-controlled Schottky emission, we develop a retention model for ferroelectric diodes. Experimentally, the metal/BFO/LSMO MFM structures with BFO thicknesses of 10, 20, 30, and 40 nm and the top electrodes of Au, Co, and Ag are prepared and their RS properties are investigated. All the structures exhibit switchable diodelike RS behaviors, where the transition from HRS to LRS is triggered by the polarization switching. The retention test on the Au/BFO(30 nm)/LSMO structure shows that the current in the LRS decays over time (i.e., resistance relaxation). Such resistance relaxation is not caused by the capacitive current from polarization relaxation or the defects-mediated charge-trapping processes, and additionally it is not observed in the nonferroelectric STO films. Because of these results and the nice fitting of $I(t)$ - t characteristics to our retention model, it is likely that the resistance relaxation is due to the polarization relaxation-induced Schottky barrier variation during the conduction. Moreover, the resistance relaxation rate becomes higher as the BFO thickness decreases from 40 to 10 nm and as the top electrode changes from Ag to Au and to Co. This suggests that the E_{dp} , which depends on the BFO thickness and the screening ability of the top electrode, plays the key role in the resistance relaxation, which is further confirmed by fitting all the $I(t)$ - t characteristics to our retention model. Therefore, the retention loss in a ferroelectric diode can be attributed to the E_{dp} -driven polarization relaxation and its effects on the Schottky emission. In addition, our study provides some guidance for the improvement of retention properties and the nondestructive monitoring of polarization over time.

ACKNOWLEDGEMENTS

The authors thank the National Key Research Program of China (Grants No. 2016YFA0201002 and No. 2016YFA0300101), the State Key Program for Basic Researches of China (Grant No. 2015CB921202), the National Natural Science Foundation of China (Grants No. 51602110, No. 11674108, No. 51272078, and No. 51332006), the Science and Technology Planning Project of Guangdong Province (Grant No. 2015B090927006), and the Natural Science Foundation of Guangdong Province (Grant No. 2016A030308019). Z. Fan, X. Gao and X. Lu acknowledge the Project for Guangdong Province Universities and Colleges Pearl River Scholar Funded Scheme 2018, 2014, and 2016, respectively.

APPENDIX A: APPLICABILITY OF EQ. (1)

Because this study deals with semiconducting ferroelectrics, which contain defects, one may have doubts

about the applicability of Eq. (1). In fact, the bulk defects (if they carry charges of the same sign and are uniformly distributed) will not produce an overall depolarization field, and thus they will not affect Eq. (1). In addition, if the amount of interfacial trapped charges is much smaller than those of polarization charges (P) and screening charges (σ_s), Eq. (1) also remains unaffected. Below, we will use the BFO films as an example to demonstrate the applicability of Eq. (1).

The defect concentration in the BFO films are evaluated using the capacitance-voltage (C - V) measurements. For proper C - V measurements, large-area Au electrodes (approximately 100 μm in diameter) and thick BFO films (approximately 130 nm in thickness) are used. Although the samples are different from those used in the CDAFM measurements (see descriptions in Sec. III), the defect concentrations in these BFO films may still be comparable because they are prepared in the same conditions. The C - V characteristics are measured in both positive and negative voltage regions, before which the +6 and -6 V dc poling procedures are conducted, respectively. With this method, the polarization switching is avoided when measuring the C - V characteristics.

As seen from Fig. 7, the C^{-2} - V curves in the positive and negative regions show linearity. Using the slopes of the C^{-2} - V curves, the doping concentration (N_{dop}) can be further estimated by [18]

$$N_{\text{dop}} = \frac{2}{q\varepsilon_0\varepsilon_{\text{st}}[d(C^{-2})/dV]}, \quad (\text{A1})$$

where ε_{st} is the static dielectric constant of BFO (approximately 60).

The N_{dop} values obtained from the C^{-2} - V curves in the positive and negative regions are approximately 3.3×10^{18}

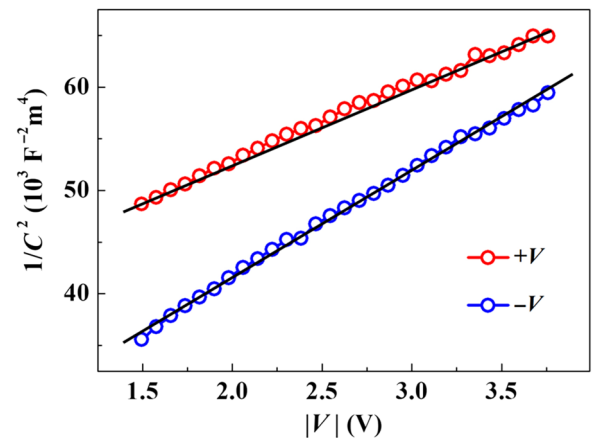


FIG. 7. C^{-2} - V plots of typical C - V characteristics measured in positive and negative voltage regions for the Au(approximately 100 μm in diameter)/BFO(approximately 130 nm in thickness)/LSMO structure.

and $2.2 \times 10^{18} \text{ cm}^{-3}$, respectively. The different N_{dop} values may be caused by the asymmetric distributions of defects near two interfaces. Hereafter, only the average value of N_{dop} (i.e., approximately $2.8 \times 10^{18} \text{ cm}^{-3}$) will be considered.

If the interfacial defect concentration (assuming that the interface region is approximately 1-nm wide) is close to N_{dop} , the resultant areal charge density is $0.045 \mu\text{C}/\text{cm}^2$, three orders of magnitude smaller than P and σ_s . Therefore, Eq. (1) applies to our BFO films. Certainly, it could be possible that the interfacial defect concentration is much larger than N_{dop} , but it can hardly reach the levels of P and σ_s (on the order of tens of $\mu\text{C}/\text{cm}^2$). Otherwise, one would observe significant defects-mediated RS behavior, which is in contradiction to the experimentally observed polarization-mediated RS behavior (see Appendix D for more discussions). Therefore, the interfacial defect concentration is not large enough to affect the applicability of Eq. (1).

APPENDIX B: CONDUCTION BEHAVIOR OF LSMO FILMS

Figure 8 demonstrates that the LSMO film exhibits metallic-conduction behavior in the temperature range of 20–320 K, because the resistivity increases with temperature. The resistivity at 300 K is approximately $0.012 \Omega \cdot \text{cm}$, which is quite low and comparable to the values reported previously [50]. In addition, the carrier concentration in the metallic LSMO film can reach approximately 10^{21} cm^{-3} [51]. Therefore, it is reasonable to treat the LSMO as a metal in the metal/BFO/LSMO heterostructures.

APPENDIX C: I - V AND I - T CHARACTERISTICS OF STO FILMS

By comparing the I - V characteristics between the STO film and the LSMO bottom electrode layer [Fig. 9(a)], one

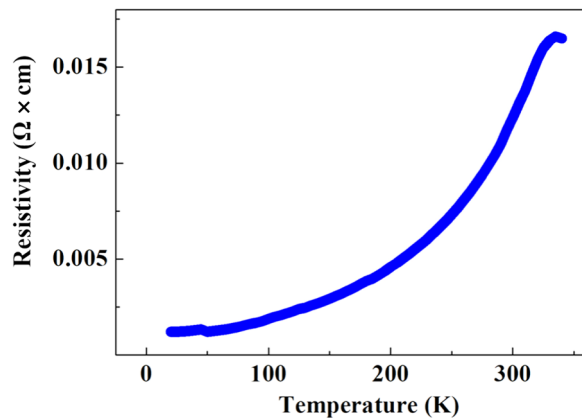


FIG. 8. Resistivity of the LSMO film as a function of temperature measured by the van der Pauw method.

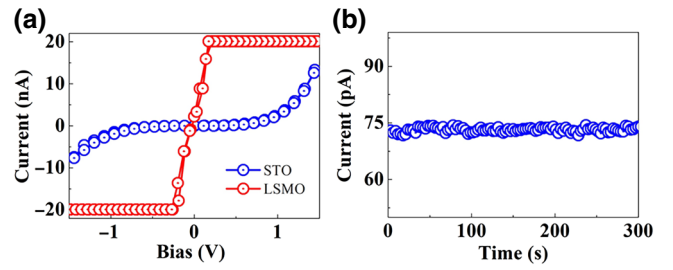


FIG. 9. (a) I - V characteristics of the nonferroelectric STO film (approximately 7 nm) and the LSMO bottom electrode layer (as a control sample). (b) $I(t)$ - t characteristics of the STO film.

can find that the STO film behaves like a resistor. Neither resistive switching [Fig. 9(a)] nor resistance relaxation [Fig. 9(b)] is observed in the STO film.

APPENDIX D: CONDUCTION MECHANISM ANALYSIS

In the MFM structures, many conduction mechanisms could work and they are classified into two categories: bulk limited and interface limited. Here, we mainly focus on the differentiation between the Schottky emission and space-charge-limited conduction (SCLC), because these two mechanisms produce good fits to the experimental I - V data (note: the Schottky emission and SCLC belong to the interface-limited and bulk-limited mechanisms, respectively). The other conduction mechanisms either produce poor fits or contradict the experimental observations, which will not be discussed hereafter.

The semi-log, log-log, and $\ln(I)$ - $V^{0.5}$ plots of the typical I - V characteristics of the Au/BFO(30 nm)/LSMO structure are presented in Figs. 10(a)–10(c), respectively. We first point out that the currents in the HRS [Fig. 10(a)] and those at low voltages (e.g., $<0.5 \text{ V}$) in the LRS [Figs. 10(b) and 10(c)] are not the true conductive currents. It seems that those currents are mainly contributed from the capacitive currents and background noises. This is because as the voltage-sweeping sequence and speed change, the sign and magnitude of the current will change (see Fig. 11). Therefore, we have not done fitting and analysis for those currents, and below we focus only on the currents at relatively large voltages in the LRS.

It is seen from Fig. 10(b) that the I - V characteristics in the log-log plot are curved, which cannot be fitted using a single line. One may still use two lines to fit the I - V curves and their slopes are calculated as approximately 2.2 and 3.7, respectively. This seems to be in agreement with the SCLC-type conduction behavior. However, it should be noted that the voltage-sweeping sequences for measuring the I - V characteristics in the LRS are $+8 \text{ V} \rightarrow 0$ and $-8 \text{ V} \rightarrow 0$, before which the voltages of $0 \rightarrow +8 \text{ V}$ and $0 \rightarrow -8 \text{ V}$ are applied, respectively. This indicates that if the SCLC works, the film would already be trap-filled

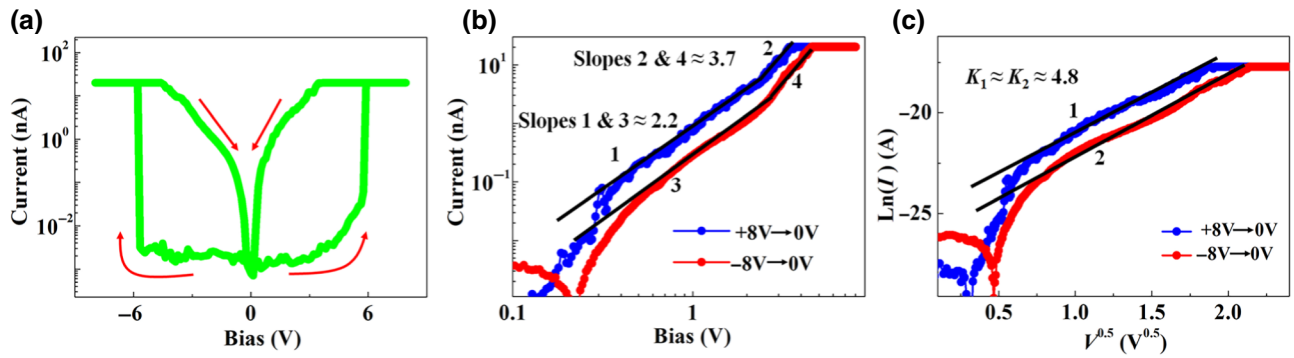


FIG. 10. (a) Semi-log, (b) log-log, and (c) $\ln(I)-V^{0.5}$ plots of the $I-V$ characteristics of the representative Au/BFO(30 nm)/LSMO structure.

when the voltage is swept back from the high voltages. In such a case, one would observe only the regions with slopes from 1 to 2 in the $I-V$ curves, while the trap-filling regions (i.e., the abruptly changing regions with slopes of approximately 3.7) would not be observed. This is, however, in contradiction to our observations.

In fact, as shown in Fig. 10(c), the $\ln(I)-V^{0.5}$ curves show linearity in wide voltage ranges. The optical dielectric constants (K) calculated from the slopes of the $\ln(I)-V^{0.5}$ curves are approximately 4.8, close to the experimental value of BFO (approximately 6.25). These results suggest that the Schottky emission may be a reasonable conduction mechanism for our Au/BFO/LSMO structures.

To further confirm that the Schottky emission rather than the SCLC is the dominant conduction mechanism, we conduct thickness-dependent $I-V$ measurements. Figure 12(a) displays the $I-V$ characteristics in the LRS for the BFO films with different thicknesses, and Fig. 12(b) further plots the current at -1 V in the LRS as a function of thickness. Clearly, the current shows a weak dependence on the BFO thickness. Such a phenomenon has been previously

observed in similar MFM structures [41,52], indicating that the conduction mechanism is interface limited rather than bulk limited (note: for the SCLC, the current varies as d^{-3} where d is the thickness [53]). Therefore, it is reasonable that the Schottky emission rather than the SCLC plays the dominant role in the conduction.

For the Schottky emission, the $I-V$ characteristics typically show significant temperature dependence, based on which one can further confirm the Schottky emission mechanism and extract the Schottky barrier heights. To measure the temperature-dependent $I-V$ characteristics, we use the conventional probe station equipped with a heater and large-area Au electrodes (approximately $100 \mu\text{m}$ in diameter). The $I-V$ characteristics are measured in both positive and negative voltage regions, before which the $+6$ and -6 V dc poling procedures are conducted, respectively. With this method, the polarization switching is avoided when measuring the $I-V$ characteristics. The measurement temperature is varied in the range of 320–390 K.

The measured $I-V$ characteristics in the positive and negative voltage regions, plotted as $\ln(J/T^2)$ vs $V^{0.5}$, are shown in Figs. 13(a) and 13(c), respectively (here, J is the current density and T is the temperature). As can be seen, the $\ln(J/T^2)-V^{0.5}$ curves show linearity in the temperature

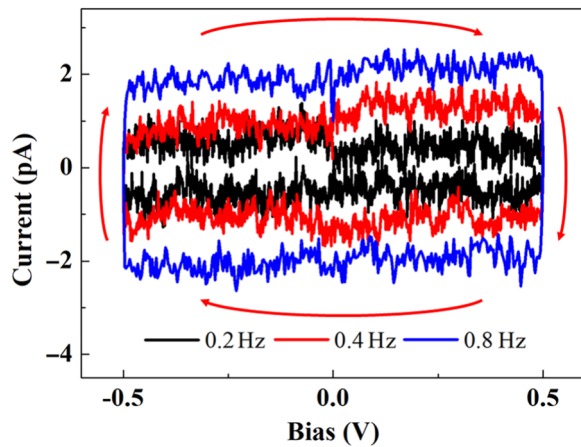


FIG. 11. $I-V$ characteristics measured in a small voltage window (<0.5 V) at different frequencies.

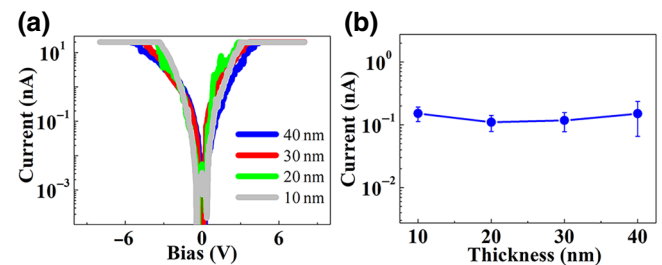


FIG. 12. (a) $I-V$ characteristics in the LRS for the BFO films with thicknesses of 10, 20, 30, and 40 nm. (b) Current measured at -1 V in the LRS as a function of thickness. For each BFO thickness, at least five devices are measured and they show similar results.

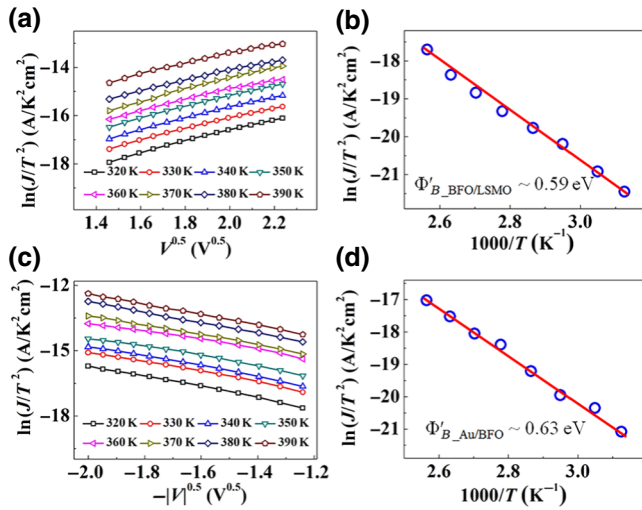


FIG. 13. Temperature-dependent I - V characteristics plotted as $\ln(J/T^2)-V^{0.5}$ in (a) positive and (c) negative voltage regions. Intercepts of linear extrapolations of $\ln(J/T^2)-V^{0.5}$ curves on the $V=0$ axis as a function of $1000/T$ in (b) positive and (d) negative voltage regions.

range of 320–390 K, indicating that the Schottky emission [i.e., Eq. (9)] is applicable.

In addition, by linearly extrapolating the $\ln(J/T^2)-V^{0.5}$ curves, one can obtain the intercepts on the $V=0$ axis. Those intercepts are plotted as a function of $1000/T$ in Figs. 13(b) and 13(d), which can be fitted using straight lines. Based on the slopes of the fitting lines, the Schottky barrier heights (Φ'_B) can be extracted. The Φ'_B values of Au/BFO and BFO/SRO barriers are calculated as approximately 0.63 and 0.59 eV, respectively. The Φ'_B values obtained here are relatively consistent with those obtained in Fig. 4(b) (approximately 0.61 eV and 0.58 eV for the Au/BFO and BFO/SRO barriers, respectively). The small deviations in Φ'_B values may be attributed to the film inhomogeneity since electrodes with different areas are used.

Last but not least, we show, in Fig. 14, that there is a distinct difference in switching sequence between the switchable diode-type RS and the SCLC-type RS. For the switchable diode-type RS, as the voltage sweeps as $-V_{\max} \rightarrow 0 \rightarrow +V_{\max} \rightarrow 0 \rightarrow -V_{\max}$, the resistance state changes as LRS \rightarrow HRS \rightarrow LRS \rightarrow HRS \rightarrow LRS. The HRS \rightarrow LRS switching occurs at the voltage where the polarization switching happens, and it can occur at both positive and negative voltage polarities. The LRS \rightarrow HRS switching occurs when the voltage goes across $V=0$ due to the current-rectifying behavior. For the SCLC-type RS, following the same voltage-sweeping sequence, however, the resistance state changes as HRS \rightarrow HRS \rightarrow LRS \rightarrow LRS \rightarrow HRS. The HRS \rightarrow LRS switching occurs at the voltage where the charge trapping occurs (e.g., at a certain positive voltage). Then, the conduction follows the trap-filled SCLC until the charge

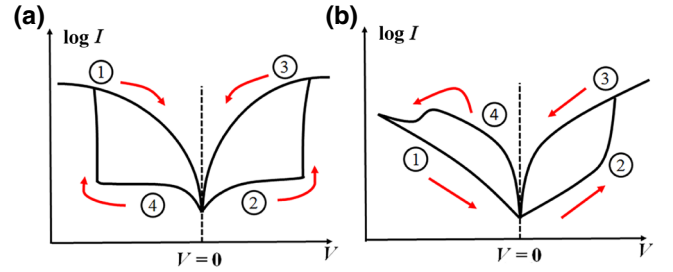


FIG. 14. Schematics showing the hysteretic I - V characteristics of (a) switchable diode-type RS and (b) SCLC-type RS.

detrapping occurs (at a certain negative voltage). After that, the conduction follows the trap-unfilled SCLC. Note that when the voltage goes across $V=0$, no change of resistance state will occur because the film remains either trap-filled or trap-unfilled.

Combining the above results and analyses, including the I - V curve fittings, thickness- and temperature-dependent I - V measurements, and switching sequences of RS, it can be concluded that the Schottky emission is the dominating conduction mechanism.

APPENDIX E: CYCLIC RETENTION TESTS

The cyclic retention tests are performed using repeated -8 V writing followed by -1 V/0 V reading, and the results are shown in Fig. 15. Figure 15(a) demonstrates that the current decay during the -1 V reading is reproducible. To understand the nature of the current measured at -1 V, a control test using a read voltage of 0 V is conducted. As seen from Fig. 15(b), the current drops to below approximately 3 pA almost instantly after the -8 V writing. This suggests that both the dielectric relaxation current and the detrapping current are very small. This further supports that the current read at -1 V [current magnitude:

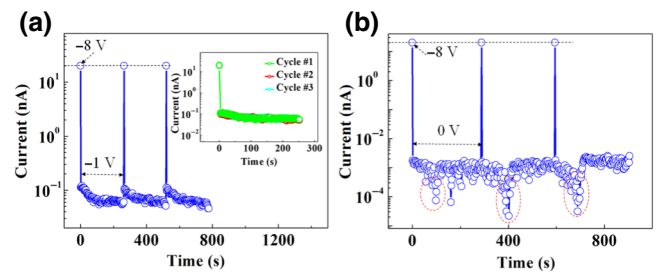


FIG. 15. Current-time (I - t) characteristics under (a) repeated -8 V writing and -1 V reading and (b) repeated -8 V writing and 0 V reading. Inset in Panel a shows the I - t characteristics for three different cycles using the moment of applying -8 V writing as the starting time. In Panels a and b, the current at -8 V reaches the compliance current (20 nA). In Panel b, the valleys indicated by red circles are caused by the very low current changing its sign.

approximately 100 pA; see Fig. 15(a)] is the conductive current rather than the dielectric relaxation current or the detrapping current.

In addition, it is observed from Fig. 15 that the current induced by a -8 V write pulse (pulse width: 1 s) reaches the compliance current, that is, 20 nA. The current induced by the -8 V write pulse mainly consists of two components: the capacitive current from the reorientation of relaxed polarization and the conductive current at -8 V. Because the conductive current at -8 V is already beyond 20 nA, observing the current peak arising from the reorientation of relaxed polarization cannot be realized in our CDAFM system.

APPENDIX F: DEFECTS-MEDIATED CHARGE TRAPPING

The defects-mediated charge trapping can be excluded as the major origin for the resistance relaxation in our Au/BFO/LSMO structures. The reasons are given as follows.

First, as shown in Fig. 5 in the main text, the resistance relaxation becomes faster as the BFO thickness decreases. If the resistance relaxation is related to the charge trapping at surface defects, the resistance relaxation rate would be weakly dependent on the BFO thickness. This can be studied by the SKPM, which probes the surface potential associated with the surface defects. As shown in Figs. 16(a)–16(c), in the 30-nm-BFO film, the surface potential of the -6 V-written region decays by approximately 30 mV after a waiting time of 10 min. Figure 16(d) further reveals that the decay of the surface potential changes very little as the BFO thickness varies. Therefore, the surface defects-mediated charge trapping results in similar relaxation behaviors in the BFO films with different thicknesses, which is inconsistent with the observed dependence of the resistance relaxation rate on the BFO thickness.

Then, the resistance relaxation is also not related to the charge trapping at bulk defects. If this was the case, the resistance relaxation would be faster in thicker BFO films. This is again in contradiction to the observed decrease of the resistance relaxation rate with BFO thickness.

Recall that the defect concentration in the BFO films evaluated by the C - V measurement is three orders of magnitude smaller than the polarization (see Appendix A for more details). In addition, the detrapping current is found to be small (Fig. 15), and no SCLC-type RS resulting from charge trapping-detrapping is observed (Fig. 14). These observations suggest that the polarization plays a much bigger role than the defects in influencing the conduction in the Au/BFO/LSMO structures.

It is noteworthy that the charge-trapping-induced resistance relaxation may not be necessarily noticeable in

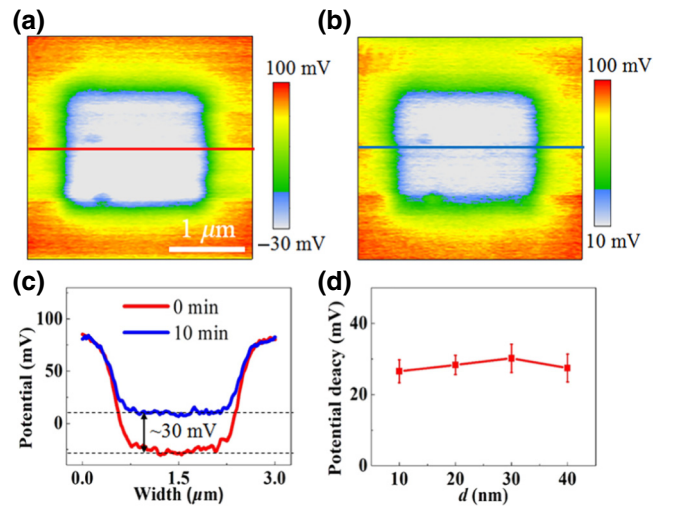


FIG. 16. SKPM images taken for the 30-nm-BFO film (a) right after writing the middle square region with -6 V and (b) after waiting for 10 min. (c) Surface potential profiles along the lines indicated in Panels a and b. (d) Potential decays measured in the BFO films with different thicknesses (waiting time: 10 min for all the films).

high-quality films. For example, the Au/STO/LSMO heterostructures, in which the STO films and electrodes are prepared using the same methods as those for the BFO-based heterostructures, do not exhibit any RS and current-decay behavior (see Fig. 9). This also hints that the polarization is correlated with the resistance relaxation, because the most distinct difference between BFO and STO is the polarization.

In view of all of the above reasons, we think that the current decay in our BFO films is not caused by the defects-mediated charge trapping, but is mainly due to the polarization relaxation and its modulations on the conduction.

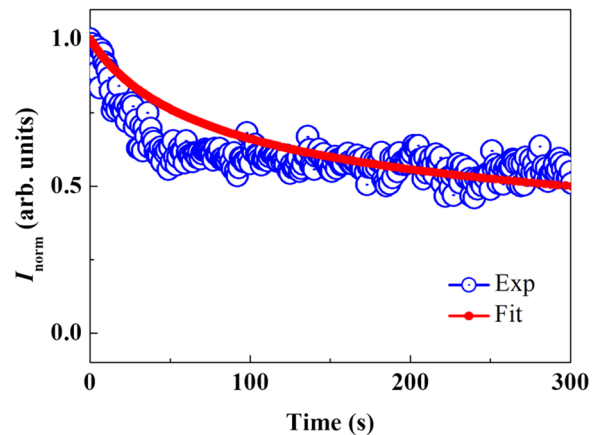


FIG. 17. $I(t)$ - t characteristics in the LRS in P_{down} state for the 30-nm-BFO film.

APPENDIX G: I - T CHARACTERISTICS OF BFO FILMS IN P_{DOWN} STATE

To achieve the LRS in the P_{down} state, the +1 V read voltage is applied after using a +8 V write pulse to set the P_{down} state. The measured I - t characteristics shown in Fig. 17 reveal a resistance-relaxation behavior.

APPENDIX H: FITTING PARAMETERS

Using Eqs. (1)–(10) and the parameter values tabulated in Table I, one can fit the I - t characteristics of metal/BFO/LSMO structures with different BFO thicknesses and different electrodes.

TABLE I. Parameters used in the fittings for the I - t characteristics of metal/BFO/LSMO structures with different BFO thicknesses and different electrodes. In the third column, “F” in the parentheses denotes that the value is fixed, while “V” denotes that the value is varied in order to obtain a good fit.

	Parameters	Values
BFO films	$P(t=0)$ ($\mu\text{C}/\text{cm}^2$)	60 (F)
	ϵ_{st}	60 (F)
	K	6.25 (F)
	t_{∞} (ns)	1 (F)
	α of 10-nm BFO (10^9 V/m)	5.2 (V)
	α of 20-nm BFO (10^9 V/m)	2.9 (V)
	α of 30-nm BFO (10^9 V/m)	2.19 (V)
	α of 40-nm BFO (10^9 V/m)	1.78 (V)
Electrodes	l_1 of LSMO (\AA)	0.8 (F)
	$\epsilon_{M,1}$ of LSMO	8 (F)
	$l_2/\epsilon_{M,2}$ of Au (\AA)	0.25 (V)
	$l_2/\epsilon_{M,2}$ of Ag (\AA)	0.24 (V)
	$l_2/\epsilon_{M,2}$ of Co (\AA)	0.281 (V)
Schottky barriers	$\Phi'_{B,2}(t=0)$ of Au/BFO(10 nm) (eV)	0.604 (V)
	$\Phi'_{B,2}(t=0)$ of Au/BFO(20 nm) (eV)	0.612 (V)
	$\Phi'_{B,2}(t=0)$ of Au/BFO(30 nm) (eV)	0.610 (V)
	$\Phi'_{B,2}(t=0)$ of Au/BFO(40 nm) (eV)	0.604 (V)
	$\Phi'_{B,2}(t=0)$ of Ag/BFO(30 nm) (eV)	0.577 (V)
	$\Phi'_{B,2}(t=0)$ of Co/BFO(30 nm) (eV)	0.598 (V)

- [1] J. F. Scott, Application of modern ferroelectrics, *Science* **315**, 954 (2007).
- [2] T. Choi, S. Lee, Y. J. Choi, V. Kiryukhin, and S. W. Cheong, Switchable ferroelectric diode and photovoltaic effect in BiFeO₃, *Science* **324**, 63 (2009).
- [3] A. Q. Jiang, C. Wang, K. J. Jin, X. B. Liu, J. F. Scott, C. S. Hwang, T. A. Tang, H. Bin Lu, and G. Z. Yang, A resistive memory in semiconducting BiFeO₃ thin-film capacitors, *Adv. Mater.* **23**, 1277 (2011).
- [4] Z. Fan, H. Fan, Z. Lu, P. Li, Z. Huang, G. Tian, L. Yang, J. Yao, C. Chen, D. Chen, Z. Yan, X. Lu, X. Gao, and J.-M. Liu, Ferroelectric Diodes With Charge Injection and Trapping, *Phys. Rev. Appl.* **7**, 014020 (2017).
- [5] M. Y. Zhuravlev, R. F. Sabirianov, S. S. Jaswal, and E. Y. Tsymlal, Giant Electroresistance in Ferroelectric Tunnel Junctions, *Phys. Rev. Lett.* **94**, 246802 (2005).
- [6] V. Garcia, S. Fusil, K. Bouzehouane, S. Enouz-Vedrenne, N. D. Mathur, A. Barthelemy, and M. Bibes, Giant tunnel electroresistance for non-destructive readout of ferroelectric states, *Nature* **460**, 81 (2009).
- [7] A. Chanthbouala, A. Crassous, V. Garcia, K. Bouzehouane, S. Fusil, X. Moya, J. Allibe, B. Dlubak, J. Grollier, S. Xavier, C. Deranlot, A. Moshar, R. Proksch, N. D. Mathur, M. Bibes, and A. Barthelemy, Solid-state memories based on ferroelectric tunnel junctions, *Nat. Nanotechnol.* **7**, 101 (2012).
- [8] D. Pantel, S. Goetze, D. Hesse, and M. Alexe, Reversible electrical switching of spin polarization in multiferroic tunnel junctions, *Nat. Mater.* **11**, 289 (2012).
- [9] J. Seidel, L. W. Martin, Q. He, Q. Zhan, Y. H. Chu, A. Rother, M. E. Hawkrige, P. Maksymovych, P. Yu, M. Gajek, N. Balke, S. V. Kalinin, S. Gemming, F. Wang, G. Catalan, J. F. Scott, N. A. Spaldin, J. Orenstein, and R. Ramesh, Conduction at domain walls in oxide multiferroics, *Nat. Mater.* **8**, 229 (2009).
- [10] L. Li, J. Britson, J. R. Jokisaari, Y. Zhang, C. Adamo, A. Melville, D. G. Schlom, L.-Q. Chen, and X. Pan, Giant resistive switching via control of ferroelectric charged domain walls, *Adv. Mater.* **28**, 6574 (2016).
- [11] H. Pang, F. Zhang, M. Zeng, X. Gao, M. Qin, X. Lu, J. Gao, Ji. Dai, and Q. Li, Preparation of epitaxial hexagonal YMnO₃ thin films and observation of ferroelectric vortex domains, *npj Quant. Mater.* **1**, 16015 (2016).
- [12] Y. Li, Y. Jin, X. Lu, J.-C. Yang, Y.-H. Chu, F. Huang, J. Zhu, and S.-W. Cheong, Rewritable ferroelectric vortex pairs in BiFeO₃, *npj Quant. Mater.* **2**, 43 (2017).
- [13] J. Jiang, Z. L. Bai, Z. H. Chen, L. He, D. W. Zhang, Q. H. Zhang, J. A. Shi, M. H. Park, J. F. Scott, C. S. Hwang, and A. Q. Jiang, Temporary formation of highly conducting domain walls for non-destructive read-out of ferroelectric domain-wall resistance switching memories, *Nat. Mater.* **17**, 49 (2018).
- [14] R. Waser and M. Aono, Nanoionics-based resistive switching memories, *Nat. Mater.* **6**, 833 (2007).
- [15] A. Sawa, Resistive switching in transition metal oxides, *Mater. Today* **11**, 28 (2008).
- [16] Z. Fan, H. Fan, L. Yang, P. L. Li, Z. X. Lu, G. Tian, Z. F. Huang, Z. W. Li, J. X. Yao, Q. Y. Luo, C. Chen, D. Y. Chen, Z. B. Yan, M. Zeng, X. B. Lu, X. S. Gao, and J.-M. Liu, Resistive switching induced by charge trapping/detrapping: A unified mechanism for colossal electroresistance in certain Nb:SrTiO₃-based heterojunctions, *J. Mater. Chem. C* **5**, 7317 (2017).
- [17] H. Fan, C. Chen, Z. Fan, L. Zhang, Z. Tan, P. Li, Z. Huang, J. Yao, G. Tian, Q. Luo, Z. Li, X. Song, D. Chen, M. Zeng, J. Gao, X. Lu, Y. Zhao, X. Gao, and J.-M. Liu, Resistive switching and photovoltaic effects in ferroelectric BaTiO₃-based capacitors with Ti and Pt top electrodes, *Appl. Phys. Lett.* **111**, 252901 (2017).
- [18] L. Pintilie and M. Alexe, Metal-ferroelectric-metal heterostructures with Schottky contacts. I. Influence of the ferroelectric properties, *J. Appl. Phys.* **98**, 124103 (2005).
- [19] D. Pantel and M. Alexe, Electroresistance effects in ferroelectric tunnel barriers, *Phys. Rev. B* **82**, 134105 (2010).
- [20] D. J. Kim, J. Y. Jo, Y. S. Kim, Y. J. Chang, J. S. Lee, J.-G. Yoon, T. K. Song, and T. W. Noh, Polarization Relaxation

- Induced by a Depolarization Field in Ultrathin Ferroelectric BaTiO₃ Capacitors, *Phys. Rev. Lett.* **95**, 237602 (2005).
- [21] A. Stamm, D. J. Kim, H. Lu, C. W. Bark, C. B. Eom, and A. Gruverman, Polarization relaxation kinetics in ultrathin ferroelectric capacitors, *Appl. Phys. Lett.* **102**, 092901 (2013).
- [22] D. Pantel, S. Goetze, D. Hesse, and M. Alexe, Room-temperature ferroelectric resistive switching in ultrathin Pb(Zr_{0.2}Ti_{0.8})O₃ films, *ACS Nano* **5**, 6032 (2011).
- [23] R. Guo, Z. Wang, S. Zeng, K. Han, L. Huang, D. G. Schlom, T. Venkatesan, Ariando, and J. Chen, Functional ferroelectric tunnel junctions on silicon, *Sci. Rep.* **5**, 12576 (2015).
- [24] H. Fan, et al., Large electroresistance and tunable photovoltaic properties of ferroelectric nanoscale capacitors based on ultrathin super-tetragonal BiFeO₃ films, *J. Mater. Chem. C* **5**, 3323 (2017).
- [25] Z. Wen, C. Li, D. Wu, A. Li, and N. Ming, Ferroelectric-field-effect-enhanced electroresistance in metal/ferroelectric/semiconductor tunnel junctions, *Nat. Mater.* **12**, 617 (2013).
- [26] W. J. Hu, Z. Wang, W. Yu, and T. Wu, Optically controlled electroresistance and electrically controlled photovoltage in ferroelectric tunnel junctions, *Nat. Commun.* **7**, 10808 (2016).
- [27] M. G. Han, M. S. Marshall, L. Wu, M. A. Schofield, T. Aoki, R. Twisten, J. Holfman, F. J. Walker, C. H. Ahn, and Y. Zhu, Interface-induced nonswitchable domains in ferroelectric thin films, *Nat. Commun.* **5**, 4693 (2014).
- [28] A. Gruverman, H. Tokumoto, A. S. Prakash, S. Aggarwal, B. Yang, M. Wuttig, R. Ramesh, O. Auciello, and T. Venkatesan, Nanoscale imaging of domain dynamics and retention in ferroelectric thin films, *Appl. Phys. Lett.* **71**, 3492 (1997).
- [29] I. B. Misirlioglu and M. Yildiz, Polarization retention and switching in ferroelectric nanocapacitors with defects on tensile substrates, *Solid-State Electron.* **38**, 67 (2012).
- [30] J. R. Arce-Gamboa and G. G. Guzmán-Verril, Random electric field instabilities of relaxor ferroelectrics, *npj Quant. Mater.* **2**, 28 (2017).
- [31] A. Gruverman and M. Tanaka, Polarization retention in SrBi₂Ta₂O₉ thin films investigated at nanoscale, *J. Appl. Phys.* **89**, 1836 (2001).
- [32] D. J. Kim, H. Lu, S. Ryu, S. Lee, C. W. Bark, C. B. Eom, and A. Gruverman, Retention of resistance states in ferroelectric tunnel memristors, *Appl. Phys. Lett.* **103**, 142908 (2013).
- [33] B. S. Kang, Jong-Gul Yoon, D. J. Kim, T. W. Noh, T. K. Song, Y. K. Lee, J. K. Lee, and Y. S. Park, Mechanisms for retention loss in ferroelectric Pt/Pb(Zr_{0.4}Ti_{0.6})O₃/Pt capacitors, *Appl. Phys. Lett.* **82**, 2124 (2003).
- [34] M. Dawber, P. Chandra, P. B. Littlewood, and J. F. Scott, Depolarization corrections to the coercive field in thin-film ferroelectrics, *J. Phys.: Condens. Matter.* **15**, L393 (2003).
- [35] R. R. Mehta, B. D. Silverman, and J. T. Jacobs, Depolarization fields in thin ferroelectric films, *J. Appl. Phys.* **44**, 3379 (1973).
- [36] X. J. Lou, Polarization retention on short, intermediate, and long time scales in ferroelectric thin films, *J. Appl. Phys.* **105**, 094107 (2009).
- [37] E. L. Colla, S. Hong, D. V. Taylor, A. K. Tagantsev, K. No, and N. Setter, Direct observation of region by region suppression of the switchable polarization (fatigue) in Pb(Zr,Ti)O₃ thin film capacitors with Pt electrodes, *Appl. Phys. Lett.* **72**, 2763 (1998).
- [38] C. S. Ganpule, V. Nagarajan, H. Li, A. S. Ogale, D. E. Steinhauer, S. Aggarwal, E. Williams, R. Ramesh, and P. De Wolf, Role of 90° domains in lead zirconate titanate thin films, *Appl. Phys. Lett.* **77**, 292 (2000).
- [39] I. Stolichnov, L. Malin, E. Colla, A. K. Tagantsev, and N. Setter, Microscopic aspects of the region-by-region polarization reversal kinetics of polycrystalline ferroelectric Pb(Zr, Ti)O₃ films, *Appl. Phys. Lett.* **86**, 012902 (2005).
- [40] A. K. Tagantsev, I. Stolichnov, N. Setter, J. S. Cross, and M. Tsukada, Non-kolmogorov-avrami switching kinetics in ferroelectric thin films, *Phys. Rev. B* **66**, 214109 (2002).
- [41] L. Pintilie, I. Vrejoiu, D. Hesse, G. LeRhun, and M. Alexe, Ferroelectric polarization-leakage current relation in high quality epitaxial Pb(Zr, Ti)O₃ films, *Phys. Rev. B* **75**, 104103 (2007).
- [42] H. Liu, K. Yao, P. Yang, Y. Du, Q. He, Y. Gu, X. Li, S. Wang, X. Zhou, and J. Wang, Thickness-dependent twinning evolution and ferroelectric behavior of epitaxial BiFeO₃ (001) thin films, *Phys. Rev. B* **82**, 064108 (2010).
- [43] G. W. Pabst, L. W. Martin, Y.-H. Chu, and R. Ramesh, Leakage mechanisms in BiFeO₃ thin films, *Appl. Phys. Lett.* **90**, 072902 (2007).
- [44] J. Wang, J. B. Neaton, H. Zheng, V. Nagarajan, S. B. Ogale, B. Liu, D. Viehland, V. Vaithyanathan, D. G. Schlom, U. V. Waghmare, N. A. Spaldin, K. M. Rabe, M. Wuttig, and R. Ramesh, Epitaxial BiFeO₃ multiferroic thin film heterostructures, *Science* **299**, 1719 (2003).
- [45] T. K. Song, S. Aggarwal, Y. Gallais, B. Nagaraj, R. Ramesh, and J. T. Evans, Activation fields in ferroelectric thin film capacitors: Area dependence, *Appl. Phys. Lett.* **73**, 3366 (1998).
- [46] W. Ji, K. Yao, and Y. C. Liang, Bulk photovoltaic effect at visible wavelength in epitaxial ferroelectric BiFeO₃ thin films, *Adv. Mater.* **22**, 1763 (2010).
- [47] A. Rana, H. Lu, K. Bogle, Q. Zhang, R. Vasudevan, V. Thakare, A. Gruverman, S. Ogale, and N. Valanoor, Scaling behavior of resistive switching in epitaxial bismuth ferrite heterostructures, *Adv. Funct. Mater.* **24**, 3962 (2014).
- [48] H. H. Wieder, Activation field and coercivity of ferroelectric barium titanate, *J. Appl. Phys.* **28**, 367 (1957).
- [49] H. B. Michaelson, Work function of elements and its periodicity, *J. Appl. Phys.* **48**, 4729 (1977).
- [50] M. Huijben, L. W. Martin, Y.-H. Chu, M. B. Holcomb, P. Yu, G. Rijnders, D. H. A. Blank, and R. Ramesh, Critical thickness and orbital ordering in ultrathin La_{0.7}Sr_{0.3}MnO₃ films, *Phys. Rev. B* **78**, 094413 (2008).
- [51] A. Ruotolo, C. Y. Lam, W. F. Cheng, K. H. Wong, and C. W. Leung, High-quality all-oxide Schottky junctions fabricated on heavily doped Nb:SrTiO₃ substrates, *Phys. Rev. B* **76**, 075122 (2007).
- [52] L. Pintilie, Advanced electrical characterization of ferroelectric thin films: Facts and artifacts, *J. Optoelectron. Adv. M* **11**, 215 (2009).
- [53] B. M. Melnick, J. F. Scott, C. A. Paz De Araujo, and L. D. McMillan, Thickness dependence of D.C. leakage current in lead zirconate-titanate (PZT) memories, *Ferroelectrics* **135**, 163 (1992).